APL Materials

Synthesis of metastable Ruddlesden–Popper titanates, $(ATiO_3)_nAO$, with $n \geq 20$ by molecular-beam epitaxy

Cite as: APL Mater. **10**, 091106 (2022); https://doi.org/10.1063/5.0101202
Submitted: 30 May 2022 • Accepted: 23 August 2022 • Published Online: 16 September 2022

Matthew R. Barone, Myoungho Jeong, Nicholas Parker, et al.

AIP Publishing

Synthesis of metastable Ruddlesden–Popper titanates, $(ATiO_3)_nAO$, with $n \geq 20$ by molecular-beam epitaxy

Cite as: APL Mater. 10, 091106 (2022); doi: 10.1063/5.0101202
Submitted: 30 May 2022 • Accepted: 23 August 2022 •
Published Online: 16 September 2022

Matthew R. Barone,[1,a)] Myoungho Jeong,[2] Nicholas Parker,[1,3] Jiaxin Sun,[1] Dmitri A. Tenne,[3] Kiyoung Lee,[2,4] and Darrell G. Schlom[1,5,6,a)]

AFFILIATIONS

[1] Department of Materials Science and Engineering, Cornell University, Ithaca, New York 14853, USA
[2] Nano Electronics Laboratory, Samsung Advanced Institute of Technology (SAIT), Samsung Electronics, 130 Samsung-ro, Yeongtong-gu, Suwon-si, Gyeonggi-do 16678, South Korea
[3] Department of Physics, Boise State University, Boise, Idaho 83725-1570, USA
[4] Department of Materials Science and Engineering, Hongik University, 94, Wausan-ro, Mapo-gu, Seoul 04066, South Korea
[5] Kavli Institute at Cornell for Nanoscale Science, Ithaca, New York 14853, USA
[6] Leibniz-Institut für Kristallzüchtung, Max-Born-Str. 2, 12489 Berlin, Germany

Note: This paper is part of the Special Topic on Materials Challenges and Synthesis Science of Emerging Quantum Materials.
[a)] **Authors to whom correspondence should be addressed:** mrb297@cornell.edu and schlom@cornell.edu

ABSTRACT

We outline a method to synthesize $(ATiO_3)_nAO$ Ruddlesden–Popper phases with high-n, where the A-site is a mixture of barium and strontium, by molecular-beam epitaxy. The precision and consistency of the method described is demonstrated by the growth of an unprecedented $(SrTiO_3)_{50}SrO$ epitaxial film. We proceed to investigate barium incorporation into the Ruddlesden–Popper structure, which is limited to a few percent in bulk, and we find that the amount of barium that can be incorporated depends on both the substrate temperature and the strain state of the film. At the optimal growth temperature, we demonstrate that as much as 33% barium can homogeneously populate the A-site when films are grown on $SrTiO_3$ (001) substrates, whereas up to 60% barium can be accommodated in films grown on $TbScO_3$ (110) substrates, which we attribute to the difference in strain. This detailed synthetic study of high n, metastable Ruddlesden–Popper phases is pertinent to a variety of fields from quantum materials to tunable dielectrics.

INTRODUCTION

Ever since the discovery of high-transition temperature (high-T_c) superconductivity in doped La_2CuO_4,[1] Ruddlesden–Popper oxides with formula $(ABO_3)_nAO$ have been an important class of compounds for condensed matter physics. These perovskite-related phases demonstrate diverse properties, including high-T_c and unconventional superconductivity,[1–5] colossal magnetoresistance,[6] exotic Mott instability,[7] metamagnetism,[8,9] electronic nematicity,[10,11] and low-loss tunable dielectricity.[12,13] Interestingly, research disproportionately focuses on the $n = 1$ and $n = 2$ members of the Ruddlesden–Popper series with chemical formula $(ABO_3)_1AO$[1–4,6,7,11] and $(ABO_3)_2AO$.[6,8–10] Attention to these series members is, at least in part, due to the amplified difficulty of synthesizing Ruddlesden–Popper phases with increasing n (excluding the $n = \infty$ perovskite phase). This difficulty is particularly obtrusive to bulk synthesis methods for which $n = 3$ is the highest value of n that has been achieved in single-phase samples of $(SrTiO_3)_nSrO$,[14] $(SrRuO_3)_nSrO$,[15] $(CaTiO_3)_nCaO$,[16] and $(LaNiO_3)_nLaO$.[17] TEM images of attempts to make bulk $(SrTiO_3)_nSrO$ phases with $n > 3$ show disordered syntactic intergrowths where n ranges from 2 to 8[18] because these phases are nearly degenerate in energy.

The highest value of n achieved to date by bulk techniques in any Ruddlesden–Popper oxide is $n = 4$[19] and for any Ruddlesden–Popper of any kind is $n = 7$.[20] For the cuprate superconductors, which have structures closely related to Ruddlesden–Popper phases,[2] the highest n of nearly single-phase samples is for the $n = 6$ phase, $HgBa_2Ca_5Cu_6O_{14+\delta}$ (Hg-1256).[21]

Accessing Ruddlesden–Popper phases with intermediate n (i.e., $4 < n < \infty$ for nickelates, ruthenates, and titanates) in oxide systems or in other homologous series is possible using thin-film methods that exploit kinetics. More specifically, the order in which precise doses of the species contained in each monolayer are supplied to the substrate can build up a targeted member of a homologous series. Nonetheless, synthesis demands precise calibration and the surface kinetics during film growth have proven counterintuitive, prompting detailed studies on Ruddlesden–Popper thin film synthesis.[22–31] Many of these studies have investigated strontium titanate Ruddlesden–Popper phases with formula $(SrTiO_3)_nSrO$ as a comparatively simple model system with no charged monolayers, no octahedral rotations, and no volatile species.[22,25–29] Nonetheless, synthetic discoveries are often transferrable across material systems. For instance, the first demonstration of the synthetically challenging superconducting $(NdNiO_3)_5NdO$ phase by MBE[5] was published only three years after the first report of superconductivity in doped $NdNiO_2$.[32] The rapid progress was, in part, facilitated by experience developed in the $(SrTiO_3)_nSrO$ system.[22,26,27] For instance, the discovery of surface rearrangement during growth of titanate Ruddlesden–Popper phases[26] was subsequently proven to apply to nickelate Ruddlesden–Popper phases as well.[27] Similarly, out-of-phase boundaries caused by atomic steps on the substrate surface were first noted in Sr_2RuO_4 films[23] due to the fragility of superconductivity in this phase. These out-of-phase boundaries are, however, observable and parasitic in many Ruddlesden–Popper thin films. Their attribution to step edges inspired minimization of this defect by implementation of creative buffer layers,[30] Ruddlesden–Popper substrates ($LaSrAlO_4$),[31] or perovskite substrates with very low miscut.[33] In summary, improved understanding of Ruddlesden–Popper synthesis and structural characterization is shared across the diverse fields for which these crystals are attractive.

In this Letter, we develop a methodology to dramatically increase the accuracy and consistency with which Ruddlesden–Popper titanate films can be grown by MBE. The precision of this methodology is used here to grow a $(SrTiO_3)_{50}SrO$ film with a 5× greater periodicity than has been reported using more conventional growth strategies.[34,35] The repeatability of this method is leveraged to study the growth window for high quality $(ATiO_3)_{20}AO$ films on $SrTiO_3$ (001) substrates, where the A-site is partially occupied by barium. We find that the structure crystallizes homogeneously with as much as 33% barium on the A-site when grown at the appropriate temperature. Note that, in bulk, only a few percent barium can be dissolved into $(SrTiO_3)_nSrO$ before second-phase inclusions of barium orthotitanate (Ba_2TiO_4) with a completely different crystal structure are observed.[36] When grown too cold, the intended horizontal double-rocksalt $(AO)_2$ Ruddlesden–Popper faults struggle to crystallize, leading to a film with mostly vertical $(AO)_2$ faults. When grown too hot, the barium does not incorporate homogenously; rather, it is partially expelled from the Ruddlesden–Popper faults leading to a sawtooth pattern in barium concentration along the growth direction. Growth on a lattice-matched substrate supresses this tendency toward inhomogeneity, enabling as much as 60% barium to be incorporated homogeneously into the Ruddlesden–Popper structure.[29] Our incorporation of metastable $(AO)_2$ faults into the perovskite $(Ba,Sr)TiO_3$ system, which is well studied for its tunable dielectric properties,[37–39] may prove a rewarding modification. Ruddlesden–Popper titanates containing all or mostly strontium are the highest performing tunable dielectrics ever measured, thanks to their extraordinarily low dielectric loss at 100 GHz,[12,13] and increasing the barium content of Ruddlesden–Popper films could enable more flexible engineering of tunability while maintaining the low dielectric loss of Ruddlesden–Popper phases. Beyond titanates, we hope that this study will increase the accessibility of other high n Ruddlesden–Popper phases and embolden researchers to consider alloying with metastable phases by employing lattice-matched substrates.

METHODS

All syntheses were performed in a Veeco Gen10 MBE system in a chamber background pressure of 5×10^{-7} Torr of (O_2 + ~10% O_3). The (001) $SrTiO_3$ substrates were terminated following the procedure developed by Koster *et al.*[40] The fluxes of strontium and barium were supplied via conventional effusion cells, and titanium was evaporated using a Ti-ball.[41] X-ray diffraction (XRD) spectra were collected using a Panalytical Empyrean diffractometer using Cu-$K_{\alpha 1}$ radiation, and atomic force microscopy (AFM) was performed using an Asylum Cypher ES Environmental AFM.

RESULTS AND DISCUSSION

Even using MBE to deliver precise monolayer doses of the constituent elements, the difficulty of synthesizing Ruddlesden–Popper films, with formula $(ABO_3)_nAO$, is amplified as n increases. In the $(SrTiO_3)_nSrO$ system, it is a common practice to calibrate the fluxes of strontium and titanium by monitoring reflection high-energy electron diffraction (RHEED) intensity oscillations during shuttering,[42,43] but the highest n ever reported using such techniques is 10, $(SrTiO_3)_{10}SrO$.[34,35] Unfortunately, we find that conventional calibration is insufficient for the consistent growth of high quality $n \geq 10$ films of $(SrTiO_3)_nSrO$. This makes studying metastable barium-containing Ruddlesden–Popper titanates with formula $(ATiO_3)_nAO$ extremely challenging because it is impossible to know whether a failed growth arose from imprecise calibration or improper growth conditions. Therefore, we begin by developing a method to consistently synthesize $(SrTiO_3)_{20}SrO$ before studying barium incorporation.

Our strategy for optimizing film stoichiometry relies on the $\sqrt{2} \times \sqrt{2}$ reconstruction that has been previously observed by reflection high-energy electron diffraction (RHEED) when $SrTiO_3$ films—grown on $(001)_p$ perovskite substrates, where the subscript p indicates pseudocubic indices—are terminated with $\gtrsim$1.2 monolayers of SrO.[44,45] This reconstruction is identified by half-order streaks that appear along the $[110]_p$ azimuth as seen in Fig. 1(d).[44,45] The appearance of a structural distortion in thin SrO epitaxially grown on $SrTiO_3$ is not surprising given that SrO is under 7.6% tensile strain when commensurately strained to $SrTiO_3$. One possible structural explanation that is consistent with the observed $\sqrt{2} \times \sqrt{2}$

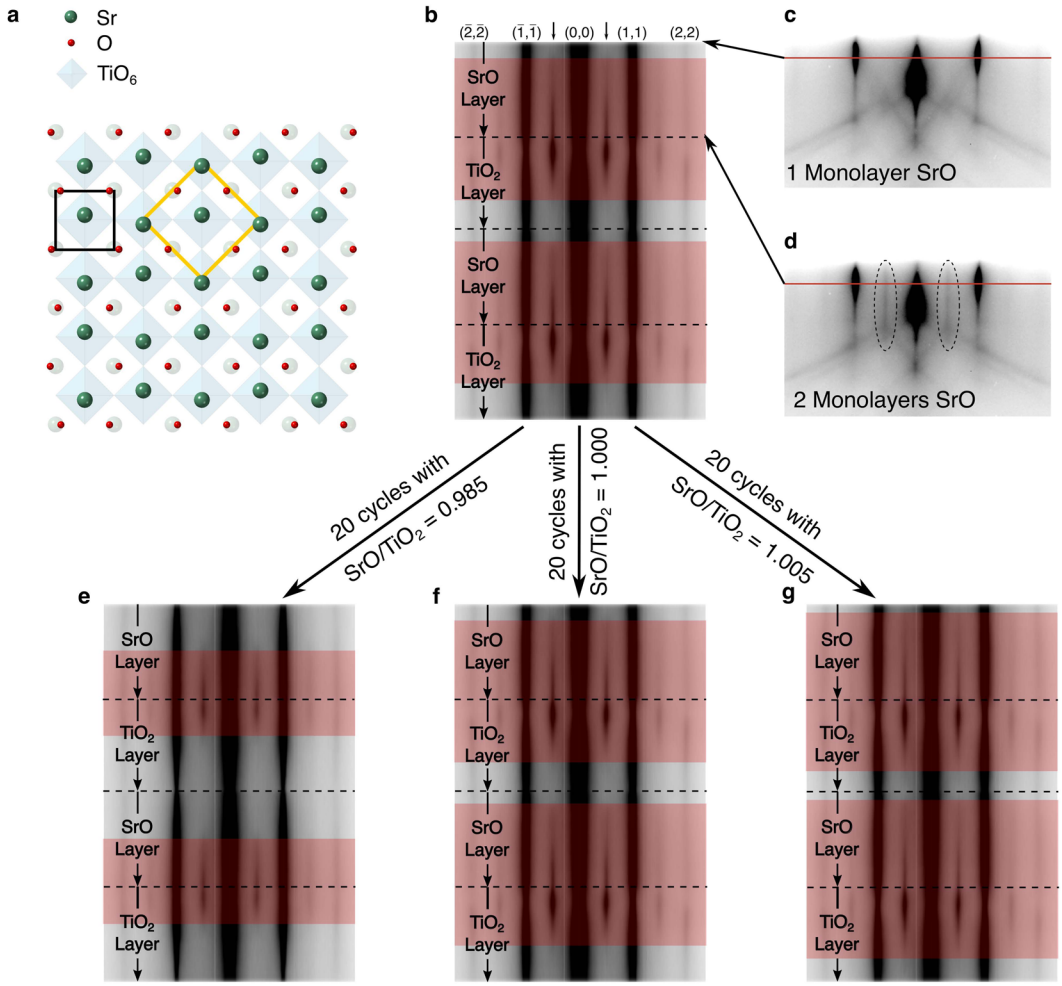

FIG. 1. (a) Proposed atomic arrangement for the $\sqrt{2} \times \sqrt{2}$ reconstruction observed when (001)-oriented $SrTiO_3$ is terminated with two monolayers of SrO. The yellow square indicates the reconstructed surface cell, and the black square indicates the bulk unit cell. (b) Line profile of the RHEED image monitored over time during the shuttered deposition of approximate monolayer doses of SrO–TiO_2–SrO–TiO_2, where shuttering steps are separated by dashed lines. The portion of the scan highlighted in red (~75% of each cycle) indicates the presence of the $\sqrt{2} \times \sqrt{2}$ reconstruction. (c) and (d) Snapshots of the RHEED pattern along the [110] azimuth when the surface is terminated with (c) 1 monolayer and (d) 2 monolayers of SrO. The red lines indicate where the line profile was collected. (e) and (f) Line profile after alternating 20 consecutive ~1 monolayer doses of SrO and TiO_2 with different dose ratios. After 20 cycles with 1.5% excess TiO_2 per cycle (e), the reconstruction is present for only ~45% of the cycle. After 20 equal doses of SrO and TiO_2 (f), the reconstruction remains present for ~75% of the cycle. After 20 cycles each with 0.5% excess SrO per cycle (e), the reconstruction is present for ~85% of the cycle.

reconstruction is suggested in Fig. 1(a), where two adjacent SrO formula units form a small cluster with interionic distances more comparable to those in bulk SrO. In addition to reconstructions, other studies have observed various nonidealities when attempting to grow SrO epitaxially on $SrTiO_3$ such as island growth after as few as two monolayers of SrO are deposited[46] and observation of (111)-oriented SrO films.[47] In the supplementary material, we characterize epitaxial SrO films that are a few monolayers thick grown on (001)-oriented $SrTiO_3$ using *in situ* RHEED at growth temperature and *ex situ* (i.e., after air exposure) atomic force microscopy (AFM) at room temperature. By AFM, we observe the onset of clear surface roughening after three monolayers of SrO are deposited, and we observe that the period of RHEED intensity oscillations during SrO deposition has a local minimum after two complete monolayers are deposited, inconsistent with what is expected[48] (and observed[49]) for RHEED oscillations from the bulk rock salt structure of SrO.

Also critical to our development of a new calibration for $(SrTiO_3)_nSrO$ films was the prior observation of layer rearrangement during growth.[26,27] It was noted that when growing $(SrTiO_3)_nSrO$ by MBE, if a TiO_2 monolayer is deposited atop two consecutive SrO monolayers, the TiO_2 will diffuse underneath; a horizontal $(AO)_2$ Ruddlesden–Popper fault only nucleates if TiO_2 is deposited atop an accumulation of three consecutive SrO monolayers on the surface

of the growing film.[26,27] Inspired by these important observations, we develop a new procedure to improve the consistency with which $(SrTiO_3)_nSrO$ can be grown by MBE.

Our strategy starts by approximating the strontium and titanium fluxes—within a few percent of actual values—using the previously developed method of monitoring RHEED intensity oscillations during shuttering.[42] With a reasonable estimate of fluxes, we start a separate procedure for fine tuning the flux measurements. We first deposit ~2 SrO monolayers atop a TiO_2-terminated $SrTiO_3$ (001) substrate,[40] and then alternately deposit monolayers of TiO_2 and SrO until the calibration is complete—usually 40–60 cycles. Assuming the initial flux approximation and surface preparation are perfect, the surface composition would oscillate between termination with 1 monolayer of SrO at the end of the TiO_2 deposition step and termination with 2 monolayers of SrO at the end of the SrO deposition step. The TiO_2 layer diffuses beneath the SrO layer, as mentioned previously, meaning that a $(SrO)_2$ Ruddlesden–Popper fault would not crystallize using this procedure.[26,27] Because the surface is terminated with >1 monolayer of SrO for most of the recipe, the $\sqrt{2} \times \sqrt{2}$ reconstruction is observable for the majority of each cycle, absent only at the end of the TiO_2 deposition and the beginning of the SrO deposition. We demonstrate this point by monitoring the line profile of the RHEED pattern along the [110] azimuth—indicated by the red line in Figs. 1(c) and 1(d)—as this recipe is run. Plotting the line profile vs time [Fig. 1(b)], we see that the half-order streaks are absent only at the end of the TiO_2 layer and the beginning of the SrO layer when the surface is terminated with approximately 1 monolayer of SrO. In addition, a video showing the appearance and disappearance of the reconstruction during this recipe is included in the supplementary material. This discussion is all assuming the fluxes are perfectly calculated, but this is not ordinarily the case.

Most likely, the SrO and TiO_2 doses are not perfectly matched, but observing the reconstruction during the calibration recipe enables quantitative determination and subsequent elimination of this nonstoichiometry. For example, if the dosage of TiO_2 is 1.5% greater than that of SrO, the $\sqrt{2} \times \sqrt{2}$ reconstruction (half-order streaks along the [110] azimuth in RHEED) will be visible for 1.5% less time each cycle. If during the first cycle the reconstruction is present for 75% of the cycle [Fig. 1(b)], then in the 20th cycle, the reconstruction will be present for only 45% of the cycle [Fig. 1(g)]; an easily observable shift results from a relatively small flux mismatch. To resolve such a flux mismatch, we could increase the strontium shutter time by 1.5% or increase the temperature of the strontium source by 0.5 °C and continue observation (at our strontium source temperature of ~500 °C the flux change is ~3%/°C).[50] Figures 1(e) and 1(f) show similar line scan evolutions for different dosage ratios. For synthesizing n = 20 Ruddlesden–Popper phases, we aim to have the flux ratios optimized to better than 0.5% or equivalently, the Sr source within 0.2 °C of the perfect flux-matching temperature. This condition is confirmed by observing <10% change in the time the reconstruction is present over the course of 20 cycles. Note that the proportional-integral-differential (PID) control of effusion cell temperatures used in this study results in temperature fluctuations of less than 0.1 °C, enabling the required precision to synthesize n = 20 Ruddlesden–Popper phases.

We find that this method of stoichiometry calibration enables more consistent synthesis of n = 20 Ruddlesden–Popper films compared to monitoring RHEED intensity oscillations during shuttered deposition alone[42] due to a number of advantages. For one, the old method is sensitive to the incident angle of the electron beam, which can easily lead to misinterpretation of the relative fluxes.[51] In addition, the updated method can be performed while rotating the substrate to ensure uniform coverage from each of the molecular beams, checking in on the [110] azimuth periodically to identify a mismatch in dosage. Most critically, this strategy gives insight into what is happening on the surface during growth of the Ruddlesden–Popper phases. This enables the grower to make adjustments that accommodate drifting fluxes or imperfect substrate termination in real time, rather than completely restarting. The advantage here is enormous when synthesizing n = 20 Ruddlesden–Popper phases for which a 1% drift in flux during the growth likely results in a failure to synthesize the target phase. An example of the drift correction protocol we employ is included in the supplementary material. Furthermore, precise termination of $SrTiO_3$ is more illusive than once believed.[52] This method is a sensitive probe of surface stoichiometry, and we find that as-prepared $SrTiO_3$ substrates are terminated with roughly 1.6 monolayers of TiO_2 rather than the commonly idealized model of single-monolayer termination. One disadvantage of our method is that if the surface is ever terminated with >2 monolayers of SrO during stoichiometry calibration, $(SrO)_2$ Ruddlesden–Popper formation or excessive surface roughening[46] may occur, frustrating the calibration method. For this reason, we begin with a condition that we know is slightly TiO_2-rich (i.e., oscillating between termination with 0.9 monolayers of SrO and 1.9 monolayers of SrO during which the $\sqrt{2} \times \sqrt{2}$ reconstruction is present for 70% of the cycle) and slowly approach perfect stoichiometry. The method can also produce unclear results for slow growth rates (>30 s/monolayer) or very high substrate temperatures (>850 °C), both of which we attribute to an increased adatom diffusion length enabling excessive roughening of the SrO-rich surface. Note that SrO grown epitaxially on $SrTiO_3$ has a tendency to roughen as discussed in the supplementary material and Ref. 46.

While the stoichiometry (or flux ratio) is precisely determined by this method, it remains to calibrate the absolute flux of the elements to enable a precise Ruddlesden–Popper film. The n values of the Ruddlesden–Popper phases adjacent to the n = 20 Ruddlesden–Popper (i.e., n = 19 and n = 21) differ by only 5%, meaning that if the stoichiometry is correct, but the absolute fluxes are 5% too high that an n = 21 film will be grown when attempting an n = 20 film. To precisely calibrate the absolute flux, we utilize an *ex situ* x-ray diffraction (XRD) approach developed previously to measure the periodicity of a Ruddlesden–Popper film so that the subsequent film can be quantitatively corrected.[29] Typically, we perform both the stoichiometry calibration and the periodicity calibration using a single calibration sample. We first calibrate stoichiometry by shuttering the growth of a perovskite with an SrO-rich surface as shown in Fig. 1(b), and adjusting source temperatures until the $\sqrt{2} \times \sqrt{2}$ reconstruction disappears when the TiO_2 layer is 80% complete for 20 consecutive cycles with the same programmed shutter time and source temperatures. Then on top of this homoepitaxial perovskite calibration layer, we deposit a 30–40 nm thick Ruddlesden–Popper film of the target series member,[22,26] measure the periodicity with

XRD, and scale the TiO_2 and SrO shutter times in subsequent films using the deviation in periodicity from the ideal structure.[29] As reported previously, to intentionally crystallize $(SrO)_2$ faults in the Ruddlesden–Popper part of the film, we periodically deposit an additional SrO monolayer so that the surface is momentarily terminated with three monolayers of SrO.[26] As discussed in the supplementary material, we believe that the surface when terminated with three monolayers of SrO is substantially rougher than previously conceived, but nonetheless, we find that this procedure enables crystallization of the intended Ruddlesden–Popper phase.

The above procedure was developed at a substrate temperature of 750 °C measured by an optical pyrometer operating at a wavelength of 980 nm and a 5×10^{-7} Torr background pressure of about 10% ozone (and ~90% oxygen). Next, we go on to study the growth window for $(SrTiO_3)_{20}SrO$ films, performing a series of growths at different substrate temperatures while keeping the ozone pressure constant (Fig. 2). To reduce the probability of misinterpretation, we perform the growths in a random order on a single day and begin each growth with the stoichiometry calibration described previously to ensure that the source fluxes have not drifted between growths. For substrate temperatures lower than 740 °C, we see that the Ruddlesden–Popper peaks anticipated in XRD are absent, but the film peak nonetheless exhibits clear Laue oscillations. Above 860 °C, Ruddlesden–Popper peaks are visible in XRD, but Laue oscillations are absent. Using the previously established method for assessing the periodicity of Ruddlesden–Popper superlattices,[29] we find films grown at 875, 825, and 775 °C had periodicities (Λ) of 16.69, 16.08, and 16.21 nm, respectively, corresponding to correction factors ($c = \frac{\Lambda}{\Lambda_{Ideal}}$) of 1.038, 0.999, and 1.008. The highest quality $(SrTiO_3)_{20}SrO$ films were grown between 740 and 850 °C on (001)-oriented $SrTiO_3$ substrates.

To investigate the cause of failure outside this temperature window, we use a combination of *in situ* RHEED during growth and *ex situ* AFM after growth. Measuring AFM on samples grown at too high a temperature, we see large precipitates on the surface, whereas for temperatures that are too low, we observe pits [Figs. 2(c)–2(f)]. Precipitates have previously been associated with SrO-rich $SrTiO_3$ surfaces, whereas pits have been observed for TiO_2-rich $SrTiO_3$ surfaces.[46,53] The observation of pits is initially surprising as all Ruddlesden–Popper compounds have excess SrO when compared to the perovskite $SrTiO_3$ phase.

To get more insight, we monitor the $\sqrt{2} \times \sqrt{2}$ reconstruction during growth to understand how the surface stoichiometry evolves throughout the synthesis. Even for the best films, we always observe that after a $(SrO)_2$ Ruddlesden–Popper fault is crystallized (i.e., after momentarily terminating the surface with three monolayers of SrO), the reconstruction persists for the entirety of the next approximately five perovskite unit cells. This observation suggests that immediately after $(SrO)_2$ crystallization the surface has more SrO than the idealized growth in which a continuous $(SrO)_2$ fault is crystallized, and the surface stoichiometry again alternates between termination with one monolayer of SrO at the end of a TiO_2 deposition step and two monolayers of SrO at the end of a SrO deposition step. After approximately five perovskite unit cells, the $\sqrt{2} \times \sqrt{2}$ reconstruction begins to disappear near the end of the TiO_2 dose, and subsequently, the reconstruction is observed less time each cycle, indicating that the SrO-excess on the surface is slowly diminished. We interpret this observation as evidence that the $(SrO)_2$ Ruddlesden–Popper fault that we intend to deposit is incomplete; it does not cover the full surface of the sample, leading to an initial excess of uncrystallized SrO adatoms on the surface. We attribute the incomplete crystallization of $(SrO)_2$ faults to roughness and stoichiometric inhomogeneity on the surface of the film. Comparing the AFM images of Ruddlesden–Popper films in Figs. 3(c)–3(f) to that of 3 monolayers of epitaxial SrO in Fig. S1(k), it is clear that surface inhomogeneity is

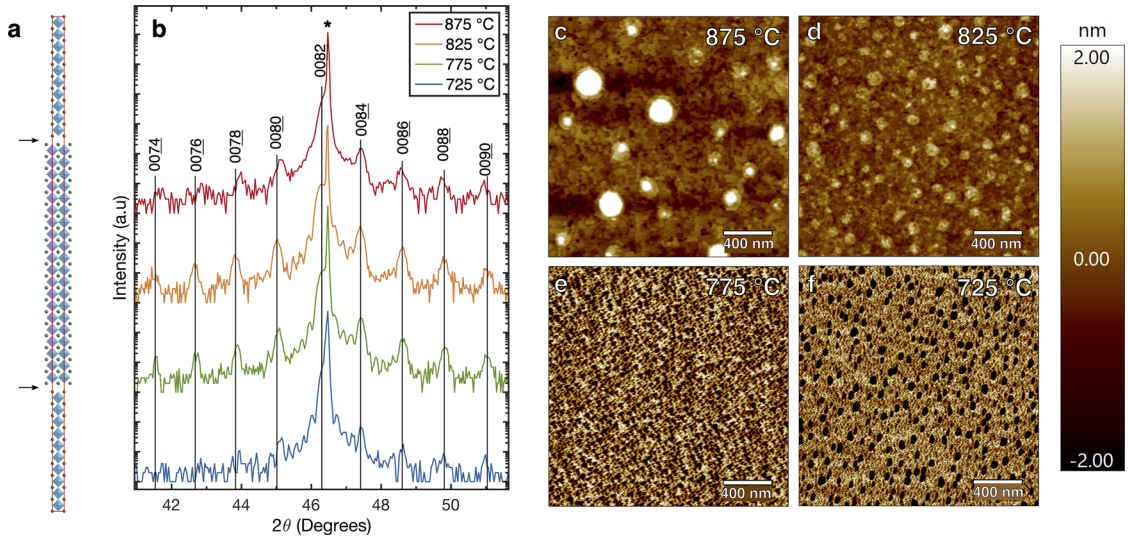

FIG. 2. (a) Unit cell of the $(SrTiO_3)_{20}SrO$ phase. Green spheres correspond to strontium atoms, TiO_6 octahedra are colored blue, and double SrO layers [which we refer to as $(SrO)_2$ faults] are indicated by arrows. (b) XRD θ-2θ scans of a series of $(SrTiO_3)_{20}SrO$ films attempted at various substrate temperatures. Vertical lines indicate the ideal peak positions. AFM images of the corresponding samples are shown in (c)–(f).

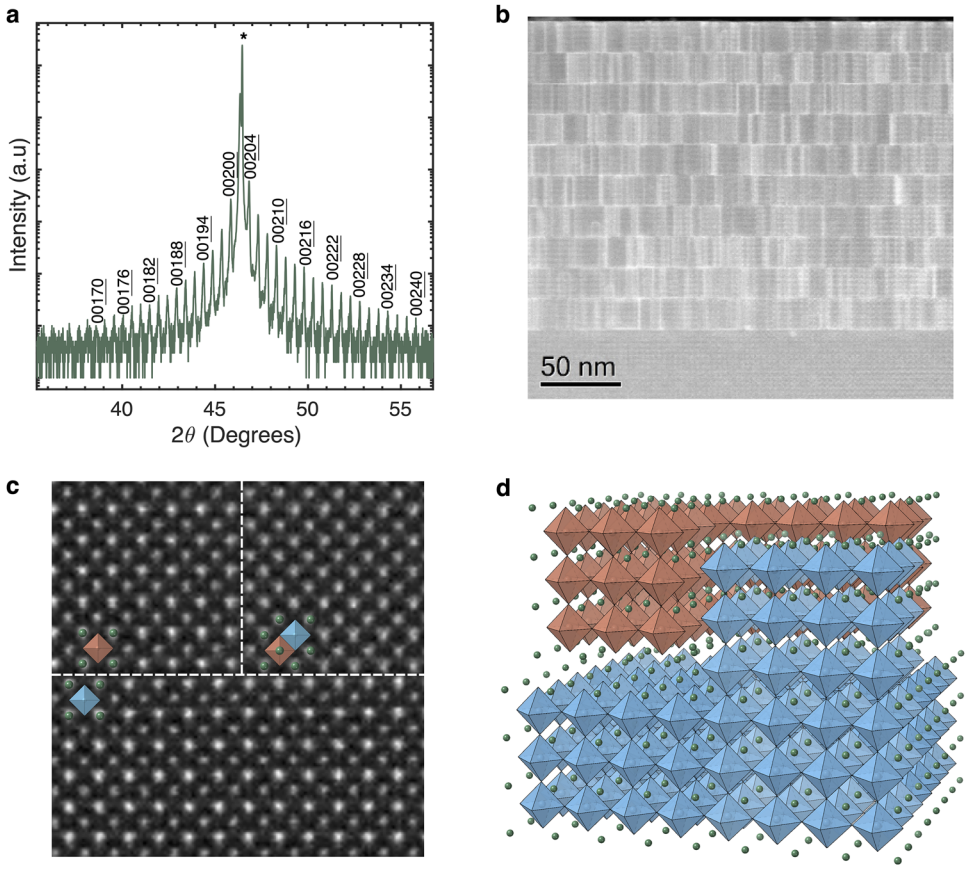

FIG. 3. (a) XRD θ-2θ scan of a 200 nm thick $(SrTiO_3)_{50}SrO$ film grown on $SrTiO_3$ (001). (b) LAADF-STEM image of the same film. (c) HAADF-STEM image and (d) atomic model of a region in which a vertical fault that does not extend through the entire lamella intersects a horizontal fault [$(SrO)_2$ faults are indicated by white dashed lines in (c)]. TiO_6 octahedra on one side of the $(SrO)_2$ antiphase boundary are shaded blue, TiO_6 octahedra on the other side are shaded orange, and all strontium ions are symbolized by green spheres.

compounded during film growth. We conjecture that as surface inhomogeneity develops, the excess SrO required for crystallization fails to diffuse to precisely where it is needed to form a perfect $(SrO)_2$ fault.

Due to the topology of $(SrO)_2$ faults, either a vertical fault or a partial dislocation with an in-plane offset of $\frac{a}{2}[110]$ must form when the intended horizontal fault is incompletely crystallized. For $n > 3$ Ruddlesden–Popper thin films, vertical faults are consistently observed,[12,13,22,24–26,28,34,54,55] whereas the authors are not aware of any studies in which faults terminated with partial dislocations are reported. We conclude that vertical faults and the RHEED observation of excess SrO on the surface after attempted crystallization of a horizontal fault are both caused by the incomplete crystallization of the horizontal fault. To clarify, we interpret that the vertical fault is structurally mandated by the incomplete horizontal fault, not induced by excess SrO on the film surface. As film growth continues, the SrO excess on the surface is slowly depleted because it is crystallized into vertical $(SrO)_2$ faults, leading to reduced presence of the $\sqrt{2} \times \sqrt{2}$ reconstruction with each perovskite cycle.

When the growth temperature is too low, the reconstruction dissipates quickly after the attempted deposition of a $(SrO)_2$ Ruddlesden–Popper fault; it is present for <50% of the 20th perovskite cycle. We interpret that, at this colder temperature, the relatively slow surface diffusion hinders the SrO from crystallizing into a horizontal fault, and thus, the extra SrO is primarily accommodated by vertical $(SrO)_2$ faults, which quickly consume the excess SrO on the surface as the film continues to grow, making the $\sqrt{2} \times \sqrt{2}$ reconstruction present for a progressively smaller fraction of each cycle. Because the excess SrO is slowly depleted with each perovskite cycle, high n films with many perovskite cycles between horizontal $(SrO)_2$ layers are less tolerant of vertical fault formation than low n films; while not systematically investigated, we believe that the lower growth temperature limit for the formation of Ruddlesden–Popper films increases with n (excluding $n = \infty$). Although the $(SrO)_2$ is not crystallized horizontally as intended when grown at a relatively low substrate temperature of 725 °C, the local lattice parameter and atomic scattering factor must remain relatively fixed throughout the thickness of film to explain the observation of Laue oscillations even though it is actually rougher by AFM than the film grown at 875 °C. Because the surface is SrO-deficient compared to the ideal case, when we attempt to terminate the film with TiO_2 at the end of the growth, we actually create a TiO_2-rich surface explaining the observation of pits in AFM at low growth temperatures.[53] Conversely, if the temperature is too hot, we see more dramatic surface roughening and eventually precipitation of SrO on the surface. We interpret that Laue oscillations in XRD are suppressed because there is an inhomogeneous distribution of $(SrO)_2$ faults due to the persistence of these large SrO islands throughout the growth, i.e., we anticipate that more $(SrO)_2$ crystallizes near these large SrO islands than far away from them, resulting in a varying local lattice parameter and atomic scattering factor.

Our observation that rather high growth temperatures are required to synthesize highly ordered $(SrTiO_3)_nSrO$ thin films is consistent with previous reports.[22,25,28] We posit that the dynamic layer rearrangement required to crystallize the target phase[26,27] requires high temperatures to overcome the energy barrier of out-of-plane diffusion. Interestingly, one previous study reported that the most successful growth of $(SrTiO_3)_5SrO$ occurs at the relatively low temperature of 550 °C by pulsed-laser deposition (PLD).[54] In their work, Iwazaki *et al.* suggest that lower substrate temperatures are necessary to avoid island growth of the SrO layer but comment that such low temperatures result in poor crystallinity. It is also possible that at 550 °C, no layer rearrangement occurs, enabling growth of low-crystallinity Ruddlesden–Popper films with the intuitive sequence of layers (i.e., with no layer rearrangement). Had this study investigated temperatures higher than 650 °C, it may have concluded that high-crystallinity Ruddlesden–Popper films could be synthesized at substrate temperatures sufficiently high to enable complete layer rearrangement.

At the optimal temperature of 810 °C, we showcase the strength of our methodology by synthesizing an $n = 50$, $(SrTiO_3)_{50}SrO$ film. The film is characterized in reciprocal space with XRD [Fig. 3(a)] and in real space with low-angle annular dark field scanning transmission electron microscopy (LAADF-STEM) [Fig. 3(b)]. This feat surpasses the highest periodicity Ruddlesden–Popper ever reported with traditional flux calibration[34,35] by a factor of five; the previous report of an $n = 20$ film was accomplished with this new method.[29] While an $n = 20$ film can be accomplished with careful calibration, the margin for error when growing an $n = 50$ film is so small that adjustments—informed by using RHEED to monitor the $\sqrt{2} \times \sqrt{2}$ reconstruction—were required during growth to maintain the optimal surface stoichiometry. It should be noted that such adjustments most likely resulted in a film with more excess SrO than the ideal structure to compensate for the SrO consumed by vertical faults, which we see are prevalent in Fig. 3(b). Nonetheless, we determine by analyzing the XRD spectrum that ordered horizontal faults were crystallized with an astounding periodicity of 39.19 nm, <1% from the optimum value of 39.55 nm ($c = \frac{\Lambda}{\Lambda_{Ideal}} = 0.991$).[29]

We use LAADF-STEM [Fig. 3(b)] because it highlights faults even at low magnification, but interpreting these data is complicated because a STEM image is a projection of a lamella. Apparent T-junctions of $(SrO)_2$ faults, which would require a partial dislocation to form, arise when vertical $(SrO)_2$ faults do not extend through the entire thickness of the lamella. We analyze such a region more thoroughly using an atomically resolved high-angle annular dark field (HAADF)-STEM image [Fig. 3(c)]. While the $(SrO)_2$ faults are harder to identify in HAADF-STEM, we see that Ti^{4+} ions (with less intensity and a smaller ionic radius) are offset horizontally by $\frac{a}{2}[110]$ in the upper left region compared to the lower region because they are separated by an $(SrO)_2$ antiphase boundary. We refer to these $(SrO)_2$ faults as antiphase boundaries because we are only considering the offset of perovskite unit cells parallel to the $(SrO)_2$ layers; perpendicular to the $(SrO)_2$ layers they are out-of-phase boundaries. This phase difference across the boundary is indicated by the overlayed perovskite unit cells—TiO_6 octahedra with the same phase as the upper left region are shaded orange and those with the same phase as the lower region are shaded blue. In the upper right region, there is no contrast between atomic columns because the orange and blue phases are superimposed in the projection due to an $(SrO)_2$ antiphase boundary perpendicular to the viewing direction partway through the lamella in this region of the scan. Figure 3(d) is a diagram of the atomic structure resulting in the HAADF-STEM image shown in Fig. 3(c), with the same color scheme for TiO_6 octahedra on opposite sides of the $(SrO)_2$ antiphase boundary.

As vertical faults do not extend through the entire lamella, accurately deducing their density from these data is nontrivial. The difference between the actual and apparent density of vertical faults depends on both the lamella's thickness, which is ~30 nm, and the typical distance that a (100)-oriented vertical fault extends before turning 90° into a (010)-oriented vertical fault. From Fig. 3(c), we can conclude from the prevalence of apparent T-junctions that the vertical faults change direction on a substantially shorter length scale than the lamella's thickness, meaning that the vertical fault density is less than we calculate from simply counting vertical lines in Fig. 3(b) (200 μm^{-1} or 1 fault/5 nm). In the supplementary material, we work toward approximating the vertical fault density more accurately, ultimately concluding that the vertical fault density in this $n = 50$ film is roughly 90 μm^{-1}, exceeding the horizontal fault density (~51 μm^{-1}) by almost a factor of two.

Having developed a methodology to synthesize $(SrTiO_3)_{20}SrO$, we move on to the more general compound $(ATiO_3)_{20}AO$, where the *A*-site is occupied by a mixture of barium and strontium. We begin by studying the case of dilute barium concentrations grown commensurately on $SrTiO_3$ substrates, using essentially the same procedure employed for $(SrTiO_3)_{20}SrO$, with minor modifications. First, in addition to the initial flux approximation previously performed by monitoring the RHEED intensity during shuttered deposition of $SrTiO_3$, we also approximate the barium flux by shuttering $BaTiO_3$ using the same methodology. Second, when depositing an *AO* layer in the flux fine-tuning step and in the Ruddlesden–Popper growth phase of the previous technique, we deposit a mixture of SrO and BaO in the appropriate ratios. For example, to grow $(ATiO_3)_{20}AO$ with $A = Ba_{0.2}Sr_{0.8}$, for each *AO* layer in the structure, we would instead sequentially deposit 0.4 monolayers of SrO followed by 0.2 monolayers of BaO followed by 0.4 monolayers of SrO to achieve mixing of SrO and BaO in the targeted ratio. Finally, in the flux fine-tuning step, we adjust the barium and strontium dosages together—e.g., increase both the strontium and barium sources by ~1 °C to resolve a 3% TiO_2-rich condition—to adjust the total *A*-site dosage while minimizing changes in the Sr/Ba ratio.

Testing *A*-site compositions with 15% and 33% barium, we see by XRD (Fig. 4) that while the minimum growth temperature to crystallize horizontal $(AO)_2$ Ruddlesden–Popper faults remains roughly constant (~730 °C), the maximum growth temperature for films with XRD spectra indicative of the highest structural order decreases with increasing barium content. As for pure $(SrTiO_3)_{20}SrO$, one component of structural disorder is the observation of randomly distributed vertical $(AO)_2$ Ruddlesden–Popper faults instead of ordered horizontal faults [Figs. 5(a) and 5(b)]. We show by electron energy loss spectroscopy (EELS) that a different component of disorder comes from the inhomogeneous incorporation of barium on the *A*-sites in the $(ATiO_3)_{20}AO$ films [Fig. 5(c)]. The effect of these two types of disorder on the XRD are different. Randomly distributed vertical $(AO)_2$ Ruddlesden–Popper faults do not diffract because they are not periodically ordered,

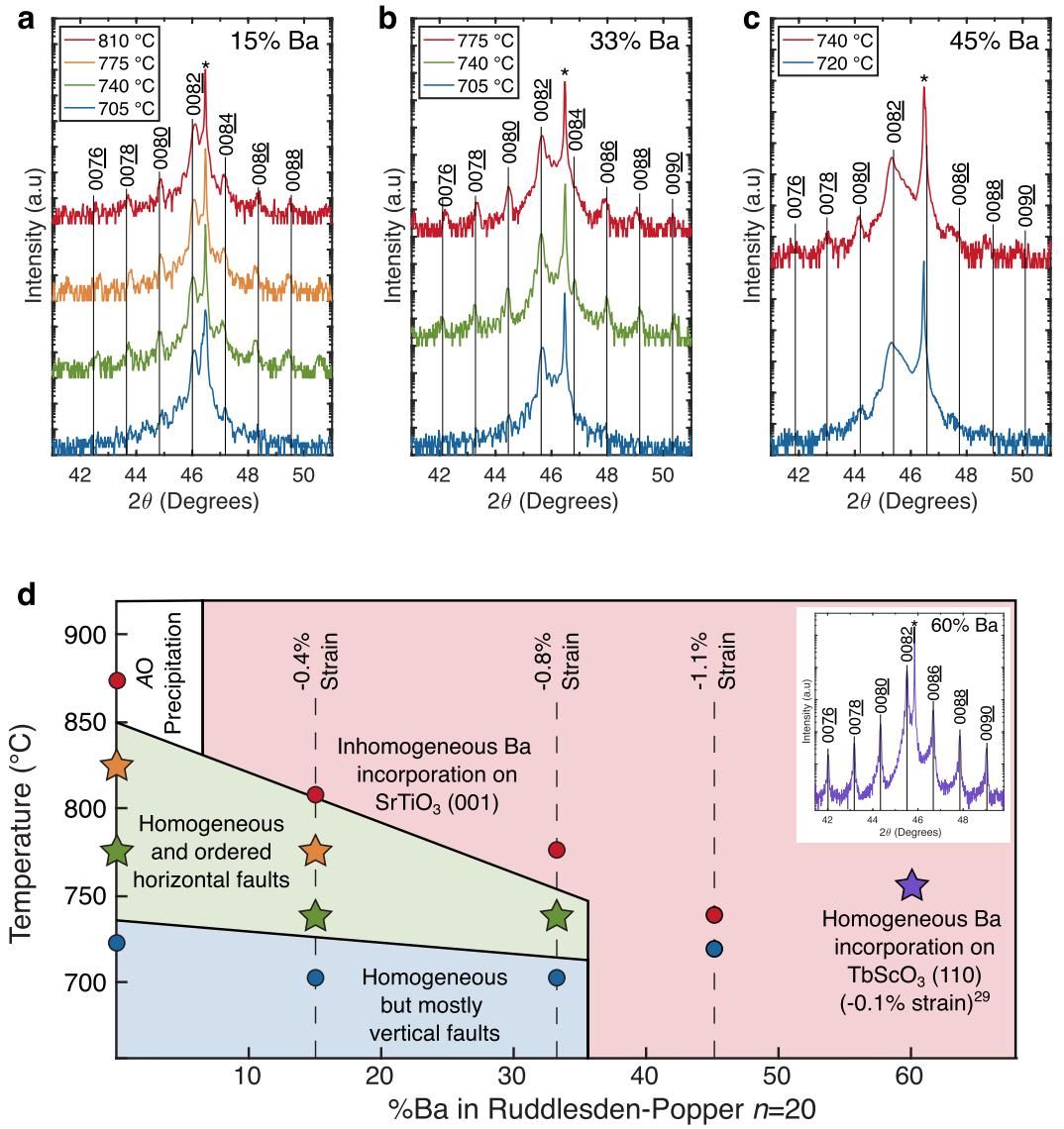

FIG. 4. (a)–(c) XRD θ-2θ scans for a series of $(ATiO_3)_{20}AO$ films grown at different temperatures with barium concentrations of 15%, 33%, and 45%, respectively, on $SrTiO_3$ (001) substrates. (d) Diagram summarizing the optimal growth conditions for the growth of $(ATiO_3)_{20}AO$ films on $SrTiO_3$ (001) substrates as a function of barium content and substrate temperature. The color of each data point corresponds to the color of the film's XRD spectrum in Figs. 2(b) and 4(a)–4(c). Starred data points indicate conditions for which the highest quality films were synthesized, and the region shaded green indicates the "growth window" in which high quality films can be synthesized on $SrTiO_3$ (001) substrates. The purple star outside the growth window marks the growth conditions with which a high quality $(ATiO_3)_{20}AO$ film was grown on a $TbScO_3$ (110) substrate (from Ref. 29), and the inset shows the corresponding XRD θ-2θ scan of the previously reported film.

meaning that no superlattice peaks are observed in such films, and the diffraction pattern resembles perovskite. For such films, i.e., those grown at substrate temperatures below 730 °C, we observe that Laue oscillations persist because the film has roughly the same out-of-plane lattice constant and local atomic scattering factor throughout its thickness. Inhomogeneous barium incorporation on the *A*-sites washes out the Laue oscillations because the local atomic scattering factor and local atomic spacing varies through the film's thickness, while the superlattice peaks remain present because the Ruddlesden–Popper faults are periodically ordered.

For $(ATiO_3)_{20}AO$ films with 15% Ba on the *A*-site, we begin to see barium inhomogeneity at 810 °C—based on the slightly misshapen 0082 peak and diminished Laue oscillations in the XRD θ-2θ scan—compared to 0% Ba films in which a well-ordered film was grown at 825 °C. Increasing the *A*-site occupancy to 33% Ba, we see clear loss of the Laue oscillations (due to barium inhomogeneity) at

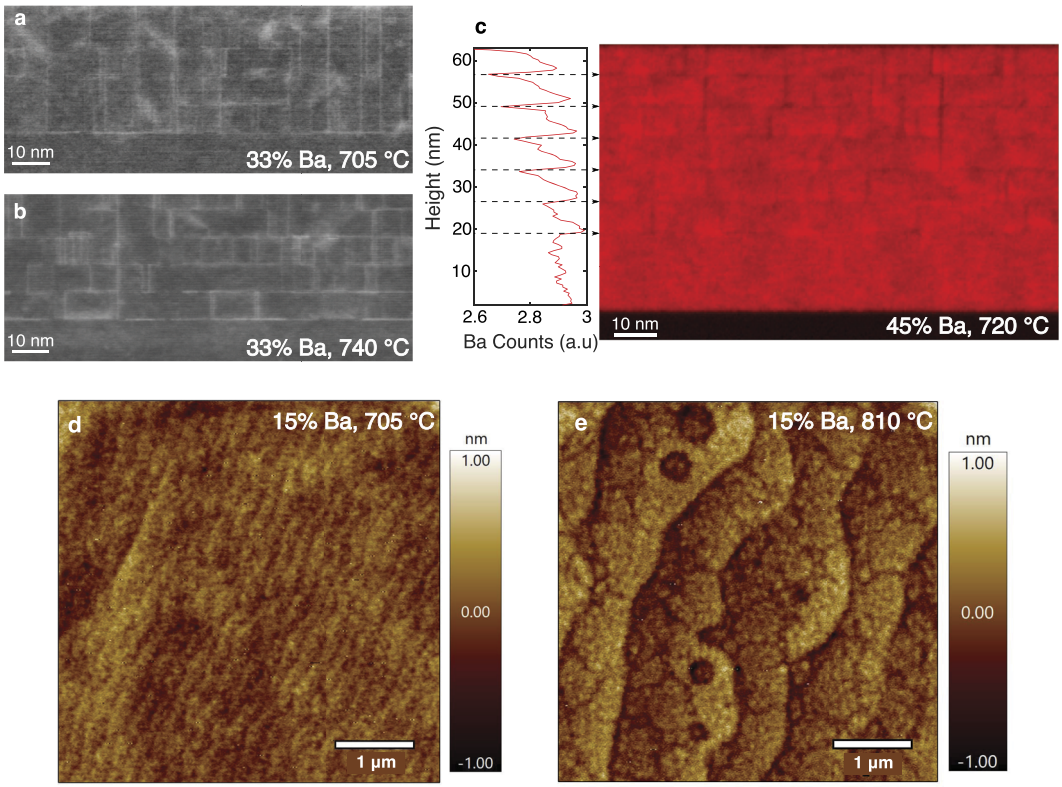

FIG. 5. LAADF-STEM images of the $(ATiO_3)_{20}AO$ films containing 33% barium grown on $SrTiO_3$ (001) at a substrate temperature of (a) 705 °C and (b) 740 °C. (c) EELS map of the $(ATiO_3)_{20}AO$ film containing 45% barium grown on a $SrTiO_3$ (001) at a substrate temperature of 720 °C. (d) and (e) AFM images of $(ATiO_3)_{20}AO$ films containing 15% Ba grown at (d) 705 °C and (e) 810 °C on $SrTiO_3$ (001).

as low as 775 °C, and attempting 45% Ba we observe dramatic loss of the Laue oscillations at only 720 °C. Note that the superlattice peaks remain relatively sharp despite the loss of the Laue oscillations in these samples that are grown at higher than optimal substrate temperature. Interestingly, we find that XRD θ-2θ scans of samples with inaccurate periodicity are qualitatively similar to those with precise periodicity, provided that the A/Ti stoichiometry is accurate, and the substrate temperature is at least 740 °C. Even though the 15% barium $(ATiO_3)_{20}AO$ films grown at 810, 775, and 740 °C have errant periodicities (16.60, 17.08, and 16.96 nm with correction factors of 1.027, 1.057, and 1.049, respectively), the superlattice peaks are clear, and the Laue oscillations are strong when grown at appropriate temperatures. The 33% barium $(ATiO_3)_{20}AO$ films grown at 775 and 740 °C have periodicities of 16.82 and 16.24 nm corresponding to correction factors of 1.032 and 0.997, respectively, and the 45% barium $(ATiO_3)_{20}AO$ film grown at 740 °C has a periodicity of 17.12 nm corresponding to a correction factor of 1.043.

When discussing the $(SrTiO_3)_{20}SrO$ films, we argued that at lower temperatures, the $(SrO)_2$ Ruddlesden–Popper faults that formed were mostly vertical and that the inhomogeneity observed at growth temperatures above 850 °C was a result of the formation of large SrO islands. With the introduction of barium, we still observe mostly vertical faults at low temperatures [Figs. 5(a) and 5(b)], but interestingly, AFM indicates that films containing only 15% barium [Figs. 5(d) and 5(e)] are much smoother at all temperatures investigated than those containing 0% barium [Figs. 2(c)–2(f)]. Therefore, we do not anticipate that the imperfection observed at high temperatures in barium-containing films has the same origin as that in pure $(SrTiO_3)_{20}SrO$. The stark difference in surface morphology for barium-containing films is possibly related to the reduced lattice mismatch of 5.7% for $Ba_{0.15}Sr_{0.85}O$ on (001)-oriented $SrTiO_3$. Notably, epitaxial BaO is known to grow smoothly on (001)-oriented $SrTiO_3$ with only −0.2% lattice mismatch.[56] Here, we analyze STEM and electron energy loss spectroscopy (EELS) of films grown outside of the growth window to better understand their imperfections. Comparing LAADF-STEM of the 33% barium $(ATiO_3)_{20}AO$ films grown at substrate temperatures of 705 and 740 °C, we see in Fig. 5(a) that the sample that is grown at 705 °C has more vertical $(AO)_2$ faults. While the first horizontal $(AO)_2$ fault appears to crystallize nearly as well as the sample grown at 740 °C, the vertical faults that do form typically persist throughout the thickness of the film at 705 °C. In contrast, the film grown at 740 °C [Fig. 5(b)] has fewer vertical faults, and when they do form, they typically end—i.e., turn horizontally—with the subsequent $(AO)_2$

horizontal fault. Again, these vertical faults are always reported in $n > 3$ Ruddlesden–Popper films,[12,13,22,24–26,28,34,54,55] and their relative density compared to horizontal faults appears to increase with n.

With the introduction of barium, we observe that the barium atoms are increasingly resistant to crystallizing into the $(AO)_2$ Ruddlesden–Popper fault as strain increases, particularly at higher substrate temperatures. This can be observed in XRD spectra by the loss of Laue oscillations as the growth temperature is increased, well before the loss of the superlattice peaks. As the barium incorporation becomes inhomogeneous, it first washes out the Laue oscillations and subsequently results in the appearance of asymmetric diffraction peaks. We investigate and confirm the microscopic origin of this effect with EELS, on the 45% Ba $(ATiO_3)_{20}AO$ sample grown at 720 °C because the inhomogeneity is clear by XRD, meaning the microstructural cause should be apparent with STEM-EELS. Integrating the barium intensity observed with EELS across the film and showing the profile along the growth direction [Fig. 5(c)], the inhomogeneous incorporation of barium into the structure is clear. The concentration of barium in the $(AO)_2$ layer is substantially less than the average barium content in the film, and the barium that is rejected from the $(AO)_2$ layer causes a spike in barium concentration immediately above the fault, which manifests as a sawtooth pattern of barium concentration. This inhomogeneity is at least partially caused by the increased strain in films with increasing barium content commensurately strained to $SrTiO_3$, as our previously reported $n = 20$, 60% Ba Ruddlesden–Popper film exhibits clear Laue oscillations when grown on $TbScO_3$ (110) under only −0.1% strain.[29] We speculate that the high strain state destabilizes the metastable phase, causing displacement of barium from the Ruddlesden–Popper fault, where its incorporation is thermodynamically unfavorable, into the perovskite matrix. This rearrangement is only observed when the temperature is sufficiently high that such rearrangement is kinetically enabled. Interestingly, we note that upward diffusion of barium, i.e., in the growth direction, in $((Ba,Sr)TiO_3)_nSrO$ has been observed previously in tensile strained films—see Fig. 2(d) of Ref. 13.

CONCLUSIONS

In this work, we outline a strategy to consistently synthesize Ruddlesden–Popper titanates with long c-axis periodicities (up to 39 nm) in the growth direction. The success of the strategy described is showcased by the demonstration of a $(SrTiO_3)_{50}SrO$ film. We go on to investigate the solubility of barium and find that the A-site can be occupied by at least 33% barium for epitaxial films grown on $SrTiO_3$ substrates at the appropriate substrate temperature. Attempts to grow Ruddlesden–Popper films at substrate temperatures below 730 °C result in incomplete crystallization of horizontal $(AO)_2$ faults, leading to films with primarily $(AO)_2$ vertical faults. Films grown at too high of a temperature can suffer from nucleation of AO precipitates on the surface or inhomogeneous incorporation of barium into the crystal structure. Due to the latter observation, the upper limit for substrate temperature falls with increasing barium content. From our previous demonstration of a $(ATiO_3)_{20}AO$ Ruddlesden–Popper with 60% barium homogeneously incorporated when grown on a $TbScO_3$ (110) substrate, it is clear that the upper limit of barium solubility when $(ATiO_3)_{20}AO$ films are grown on $SrTiO_3$ at 33% barium comes from strain; more than 33% barium can be homogenously incorporated by using substrates with a larger lattice parameter. We hope this detailed study will guide future syntheses of Ruddlesden–Popper phases that were previously thought inaccessible due to metastability or inadequate calibration techniques and enable their diverse physical properties to be established and exploited.

SUPPLEMENTARY MATERIAL

The supplementary material includes a document containing data and analysis of epitaxial SrO films that are 1–3 monolayers thick grown on $SrTiO_3$ (001), a procedure for correcting flux drift, and our method for approximation of the vertical fault density in the $(SrTiO_3)_{50}SrO$ film. In addition, a video showing the appearance and disappearance of 1/2-order streaks during deposition is included.

ACKNOWLEDGMENTS

The synthesis science work at Cornell (M.B., J.S., and D.G.S.) was supported by the U.S. Department of Energy, Office of Basic Sciences, Division of Materials Sciences and Engineering, under Award No. DE-SC0002334. We also gratefully acknowledge support by Samsung Electronics Company. N.P. and D.A.T. acknowledge support by the National Science Foundation (Grant No. DMR-2104918). Sample preparation was, in part, facilitated by the Cornell NanoScale Facility, a member of the National Nanotechnology Coordinated Infrastructure (NNCI), which is supported by the National Science Foundation (Grant No. NNCI-2025233). The authors thank Sean Christopher Palmer for his assistance with substrate preparation. Some images were generated using CrystalMaker: CrystalMaker Software Ltd. (www.crystalmaker.com).

AUTHOR DECLARATIONS

Conflict of Interest

The authors have no conflicts to disclose.

Author Contributions

Matthew Barone: Conceptualization (equal); Data curation (lead); Formal analysis (lead); Investigation (lead); Methodology (lead); Visualization (lead); Writing – original draft (lead); Writing – review & editing (supporting). **Myoungho Jeong**: Formal analysis (supporting); Investigation (supporting). **Nicholas Parker**: Data curation (supporting); Investigation (supporting). **Jiaxin Sun**: Investigation (supporting). **Dmitri A. Tenne**: Funding acquisition (supporting). **Kiyoung Lee**: Funding acquisition (supporting); Resources (supporting); Supervision (supporting). **Darrell G. Schlom**: Conceptualization (equal); Formal analysis (supporting); Funding acquisition (lead); Methodology (supporting); Project administration (lead); Resources (lead); Supervision (lead); Visualization (supporting); Writing – review & editing (lead).

DATA AVAILABILITY

The data that support the findings of this study are available from the corresponding author upon reasonable request.

REFERENCES

[1] J. G. Bednorz and K. A. Müller, Z. Phys. B: Condens. Matter **64**, 189 (1986).
[2] H. Müller-Buschbaum, Angew. Chem., Int. Ed. Engl. **28**, 1472 (1989).
[3] Y. Maeno, H. Hashimoto, K. Yoshida, S. Nishizaki, T. Fujita, J. G. Bednorz, and F. Lichtenberg, Nature **372**, 532 (1994).
[4] A. P. Mackenzie and Y. Maeno, Rev. Mod. Phys. **75**, 657 (2003).
[5] G. A. Pan, D. Ferenc Segedin, H. LaBollita, Q. Song, E. M. Nica, B. H. Goodge, A. T. Pierce, S. Doyle, S. Novakov, D. Córdova Carrizales, A. T. N'Diaye, P. Shafer, H. Paik, J. T. Heron, J. A. Mason, A. Yacoby, L. F. Kourkoutis, O. Erten, C. M. Brooks, A. S. Botana, and J. A. Mundy, Nat. Mater. **21**, 160 (2022).
[6] Y. Moritomo, A. Asamitsu, H. Kuwahara, and Y. Tokura, Nature **380**, 141 (1996).
[7] B. J. Kim, H. Jin, S. J. Moon, J.-Y. Kim, B.-G. Park, C. S. Leem, J. Yu, T. W. Noh, C. Kim, S.-J. Oh, J.-H. Park, V. Durairaj, G. Cao, and E. Rotenberg, Phys. Rev. Lett. **101**, 076402 (2008).
[8] R. S. Perry, L. M. Galvin, S. A. Grigera, L. Capogna, A. J. Schofield, A. P. Mackenzie, M. Chiao, S. R. Julian, S. I. Ikeda, S. Nakatsuji, Y. Maeno, and C. Pfleiderer, Phys. Rev. Lett. **86**, 2661 (2001).
[9] S. A. Grigera, R. S. Perry, A. J. Schofield, M. Chiao, S. R. Julian, G. G. Lonzarich, S. I. Ikeda, Y. Maeno, A. J. Millis, and A. P. Mackenzie, Science **294**, 329 (2001).
[10] E. Fradkin, S. A. Kivelson, M. J. Lawler, J. P. Eisenstein, and A. P. Mackenzie, Annu. Rev. Condens. Matter Phys. **1**, 153 (2010).
[11] J. Wu, H. P. Nair, A. T. Bollinger, X. He, I. Robinson, N. J. Schreiber, K. M. Shen, D. G. Schlom, and I. Božović, Proc. Natl. Acad. Sci. U. S. A. **117**, 10654 (2020).
[12] C.-H. Lee, N. D. Orloff, T. Birol, Y. Zhu, V. Goian, E. Rocas, R. Haislmaier, E. Vlahos, J. A. Mundy, L. F. Kourkoutis, Y. Nie, M. D. Biegalski, J. Zhang, M. Bernhagen, N. A. Benedek, Y. Kim, J. D. Brock, R. Uecker, X. X. Xi, V. Gopalan, D. Nuzhnyy, S. Kamba, D. A. Muller, I. Takeuchi, J. C. Booth, C. J. Fennie, and D. G. Schlom, Nature **502**, 532 (2013).
[13] N. M. Dawley, E. J. Marksz, A. M. Hagerstrom, G. H. Olsen, M. E. Holtz, V. Goian, C. Kadlec, J. Zhang, X. Lu, J. A. Drisko, R. Uecker, S. Ganschow, C. J. Long, J. C. Booth, S. Kamba, C. J. Fennie, D. A. Muller, N. D. Orloff, and D. G. Schlom, Nat. Mater. **19**, 176 (2020).
[14] G. J. McCarthy, W. B. White, and R. Roy, J. Am. Ceram. Soc. **52**, 463 (1969).
[15] E. Carleschi, B. P. Doyle, R. Fittipaldi, V. Granata, A. M. Strydom, M. Cuoco, and A. Vecchione, Phys. Rev. B **90**, 205120 (2014).
[16] M. M. Elcombe, E. H. Kisi, K. D. Hawkins, T. J. White, P. Goodman, and S. Matheson, Acta Crystallogr., Sect. B **47**, 305 (1991).
[17] R. A. M. Ram, L. Ganapathi, P. Ganguly, and C. N. R. Rao, J. Solid State Chem. **63**, 139 (1986).
[18] R. J. D. Tilley, J. Solid State Chem. **21**, 293 (1977).
[19] S. Liu, M. Avdeev, Y. Liu, M. R. Johnson, and C. D. Ling, Inorg. Chem. **55**, 1403 (2016).
[20] C. M. M. Soe, G. P. Nagabhushana, R. Shivaramaiah, H. Tsai, W. Nie, J.-C. Blancon, F. Melkonyan, D. H. Cao, B. Traoré, L. Pedesseau, M. Kepenekian, C. Katan, J. Even, T. J. Marks, A. Navrotsky, A. D. Mohite, C. C. Stoumpos, and M. G. Kanatzidis, Proc. Natl. Acad. Sci. U. S. A. **116**, 58 (2019).
[21] A. Iyo, Y. Tanaka, H. Kito, Y. Kodama, P. M. Shirage, D. D. Shivagan, K. Tokiwa, and T. Watanabe, J. Phys.: Conf. Ser. **108**, 012046 (2008).
[22] J. H. Haeni, C. D. Theis, D. G. Schlom, W. Tian, X. Q. Pan, H. Chang, I. Takeuchi, and X.-D. Xiang, Appl. Phys. Lett. **78**, 3292 (2001).
[23] M. A. Zurbuchen, Y. Jia, S. Knapp, A. H. Carim, D. G. Schlom, and X. Q. Pan, Appl. Phys. Lett. **83**, 3891 (2003).
[24] W. Tian, J. H. Haeni, D. G. Schlom, E. Hutchinson, B. L. Sheu, M. M. Rosario, P. Schiffer, Y. Liu, M. A. Zurbuchen, and X. Q. Pan, Appl. Phys. Lett. **90**, 022507 (2007).
[25] M. Jungbauer, S. Hühn, R. Egoavil, H. Tan, J. Verbeeck, G. Van Tendeloo, and V. Moshnyaga, Appl. Phys. Lett. **105**, 251603 (2014).
[26] Y. F. Nie, Y. Zhu, C.-H. Lee, L. F. Kourkoutis, J. A. Mundy, J. Junquera, P. Ghosez, D. J. Baek, S. Sung, X. X. Xi, K. M. Shen, D. A. Muller, and D. G. Schlom, Nat. Commun. **5**, 4530 (2014).
[27] J. H. Lee, G. Luo, I. C. Tung, S. H. Chang, Z. Luo, M. Malshe, M. Gadre, A. Bhattacharya, S. M. Nakhmanson, J. A. Eastman, H. Hong, J. Jellinek, D. Morgan, D. D. Fong, and J. W. Freeland, Nat. Mater. **13**, 879 (2014).
[28] R. C. Haislmaier, G. Stone, N. Alem, and R. Engel-Herbert, Appl. Phys. Lett. **109**, 043102 (2016).
[29] M. R. Barone, N. M. Dawley, H. P. Nair, B. H. Goodge, M. E. Holtz, A. Soukiassian, E. E. Fleck, K. Lee, Y. Jia, T. Heeg, R. Gatt, Y. Nie, D. A. Muller, L. F. Kourkoutis, and D. G. Schlom, APL Mater. **9**, 021118 (2021).
[30] J. Kim, J. Mun, C. M. Palomares García, B. Kim, R. S. Perry, Y. Jo, H. Im, H. G. Lee, E. K. Ko, S. H. Chang, S. B. Chung, M. Kim, J. W. A. Robinson, S. Yonezawa, Y. Maeno, L. Wang, and T. W. Noh, Nano Lett. **21**, 4185 (2021).
[31] J. Kim, Y. Kim, J. Mun, W. J. Choi, Y. Chang, J. R. Kim, B. Gil, J. H. Lee, S. Hahn, H. Kim, S. H. Chang, G. Do Lee, M. Kim, C. Kim, and T. W. Noh, "Defect engineering in A_2BO_4 thin films via surface-reconstructed $LaSrAlO_4$ substrates" (unpublished).
[32] D. Li, K. Lee, B. Y. Wang, M. Osada, S. Crossley, H. R. Lee, Y. Cui, Y. Hikita, and H. Y. Hwang, Nature **572**, 624 (2019).
[33] C. M. P. Garcia, A. Di Bernardo, G. Kimbell, M. E. Vickers, F. C.-P. Massabuau, S. Komori, G. Divitini, Y. Yasui, H. G. Lee, J. Kim, B. Kim, M. G. Blamire, A. Vecchione, R. Fittipaldi, Y. Maeno, T. W. Noh, and J. W. A. Robinson, Commun. Mater. **1**, 23 (2020).
[34] C.-H. Lee, N. J. Podraza, Y. Zhu, R. F. Berger, S. Shen, M. Sestak, R. W. Collins, L. F. Kourkoutis, J. A. Mundy, H. Wang, Q. Mao, X. Xi, L. J. Brillson, J. B. Neaton, D. A. Muller, and D. G. Schlom, Appl. Phys. Lett. **102**, 122901 (2013).
[35] N. M. Dawley, E. K. Pek, C.-H. Lee, E. J. Ragasa, X. Xiong, K. Lee, S. R. Phillpot, A. V Chernatynskiy, D. G. Cahill, and D. G. Schlom, Appl. Phys. Lett. **118**, 091904 (2021).
[36] W. Kwestroo and H. A. M. Paping, J. Am. Ceram. Soc. **42**, 292 (1959).
[37] A. K. Tagantsev, V. O. Sherman, K. F. Astafiev, J. Venkatesh, and N. Setter, J. Electroceram. **11**, 5 (2003).
[38] P. Bao, T. J. Jackson, X. Wang, and M. J. Lancaster, J. Phys. D.: Appl. Phys. **41**, 063001 (2008).
[39] C. J. G. Meyers, C. R. Freeze, S. Stemmer, and R. A. York, Appl. Phys. Lett. **109**, 112902 (2016).
[40] G. Koster, B. L. Kropman, G. J. H. M. Rijnders, D. H. A. Blank, and H. Rogalla, Appl. Phys. Lett. **73**, 2920 (1998).
[41] C. D. Theis and D. G. Schlom, J. Vac. Sci. Technol., A **14**, 2677 (1996).
[42] J. H. Haeni, C. D. Theis, and D. G. Schlom, J. Electroceram. **4**, 385 (2000).
[43] B. A. Davidson, A. Y. Petrov, P. Torelli, F. Li, H. Shin, and Z. Zou, in International Workshop on Oxide Electronics, Kyoto, Japan, 2019.
[44] Z. Yu, Y. Liang, C. Overgaard, X. Hu, J. Curless, H. Li, Y. Wei, B. Craigo, D. Jordan, R. Droopad, J. Finder, K. Eisenbeiser, D. Marshall, K. Moore, J. Kulik, and P. Fejes, Thin Solid Films **462–463**, 51 (2004).
[45] P. Fisher, H. Du, M. Skowronski, P. A. Salvador, O. Maksimov, and X. Weng, J. Appl. Phys. **103**, 013519 (2008).
[46] F. V. E. Hensling, T. Heisig, N. Raab, C. Baeumer, and R. Dittmann, Solid State Ionics **325**, 247 (2018).
[47] T. Gagnidze, H. Ma, C. Cancellieri, G.-L. Bona, and F. La Mattina, Sci. Technol. Adv. Mater. **20**, 456 (2019).
[48] T. Terashima, Y. Bando, K. Iijima, K. Yamamoto, K. Hirata, K. Hayashi, K. Kamigaki, and H. Terauchi, Phys. Rev. Lett. **65**, 2684 (1990).
[49] J. Sun, C. T. Parzyck, J. H. Lee, C. M. Brooks, L. F. Kourkoutis, X. Ke, R. Misra, J. Schubert, F. V. Hensling, M. R. Barone, Z. Wang, M. E. Holtz, N. J. Schreiber, Q. Song, H. Paik, T. Heeg, D. A. Muller, K. M. Shen, and D. G. Schlom, Phys. Rev. Mater. **6**, 033802 (2022).
[50] R. E. Honig and D. A. Kramer, RCA Rev. **30**, 285 (1969).
[51] H. Y. Sun, Z. W. Mao, T. W. Zhang, L. Han, T. T. Zhang, X. B. Cai, X. Guo, Y. F. Li, Y. P. Zang, W. Guo, J. H. Song, D. X. Ji, C. Y. Gu, C. Tang, Z. B. Gu, N. Wang, Y. Zhu, D. G. Schlom, Y. F. Nie, and X. Q. Pan, Nat. Commun. **9**, 2965 (2018).
[52] S. Smink, W. Lin, J. Mannhart, and W. Braun, Appl. Phys. Lett. **120**, 161602 (2022).

[53]H. Ota, S. Migita, S.-B. Xiong, H. Fujino, Y. Kasai, and S. Sakai, Jpn. J. Appl. Phys., Part 2 **38**, L1535 (1999).
[54]Y. Iwazaki, T. Suzuki, S. Sekiguchi, and M. Fujimoto, Jpn. J. Appl. Phys., Part 2 **38**, L1443 (1999).
[55]W. Tian, X. Q. Pan, J. H. Haeni, and D. G. Schlom, J. Mater. Res. **16**, 2013 (2001).
[56]T. Ohnishi, M. Yoshimoto, G. H. Lee, T. Maeda, and H. Koinuma, J. Vac. Sci. Technol., A **15**, 2469 (1997).

<u>Supplemental Information:</u> Synthesis of metastable Ruddlesden-Popper titanates, $(ATiO_3)_nAO$, with $n \geq 20$ by molecular-beam epitaxy

Matthew Barone,[1] Myoungho Jeong,[2] Nicholas Parker,[3] Jiaxin Sun,[1] Dmitri A. Tenne,[3] Kiyoung Lee,[2,4] Darrell G. Schlom[1,5,6]

1. Department of Materials Science and Engineering, Cornell University, Ithaca, New York 14853, USA
2. Nano Electronics Laboratory, Samsung Advanced Institute of Technology (SAIT), Samsung Electronics, 130 Samsung-ro, Yeongtong-gu, Suwon-si, Gyeonggi-do 16678, South Korea
3. Department of Physics, Boise State University, Boise, Idaho 83725-1570, USA
4. Department of Materials Science and Engineering, Hongik University, 94, Wausan-ro, Mapo-gu, Seoul, 04066, South Korea
5. Kavli Institute at Cornell for Nanoscale Science, Ithaca, New York 14853, USA
6. Leibniz-Institut für Kristallzüchtung, Max-Born-Str. 2, 12489 Berlin, Germany

I. Characterization of few-monolayer SrO growth on $SrTiO_3$

To better understand SrO-rich surfaces, which are important to $(SrTiO_3)_nSrO$ growth, we measure reflection high energy electron diffraction (RHEED) intensity oscillations during SrO deposition on $SrTiO_3$ and conduct *ex situ* AFM measurements of epitaxial SrO films that are a few monolayers thick grown at a substrate temperature of 775 °C. By one monolayer we mean that the substrate is exposed to a strontium flux yielding a total dose of 6.56×10^{14} Sr atoms/cm^2, while being bathed in a simultaneous oxidant flux (O_2 + ~10% O_3). Interestingly, we find that the diffracted RHEED intensity along the [110] azimuth of $SrTiO_3$ (i.e., the [100] azimuth of SrO) has a local maximum after the completion of 1 SrO monolayer, a local minimum after 2 SrO monolayers, and another local maximum after 3 SrO monolayers, displaying double the periodicity that would be expected for smooth

homoepitaxial (001) SrO. We attribute the local minimum in diffracted intensity of SrO after 2 monolayers to the $\sqrt{2} \times \sqrt{2}$ reconstruction, as we see the ½-order intensity is highest after 2 monolayers are deposited based on the RHEED images in Fig. S1(d-g).

From AFM data on epitaxial SrO films that are a few monolayers thick, we find that the terrace structure of the as-prepared substrate[1] is increasingly masked by the increasing surface roughness on the terraces as SrO thickness increases. The rms roughnesses of the bare substrate, 1, 1.5, 2, and 3 monolayer thick films are 120 pm, 135 pm, 130 pm, 133 pm, and 186 pm, respectively, according to the AFM images in Fig. S1(a) and Fig. S1 (h-k). An increase in roughness with SrO thickness is seen, particularly after the deposition of 3 monolayers of SrO. The surface roughening has a small feature size of only a few nanometers, much smaller than reported previously by PLD.[2] We cannot prove that these measurements are representative of the surface *in situ*, as SrO tends to quickly form hydroxides when exposed to air, but nonetheless, they support our suggestion that epitaxial SrO on $SrTiO_3$ is prone to roughening. According to the AFM data presented in Fig. 2(c-f), this roughening likely compounds during the growth of Ruddlesden-Popper titanate phases.

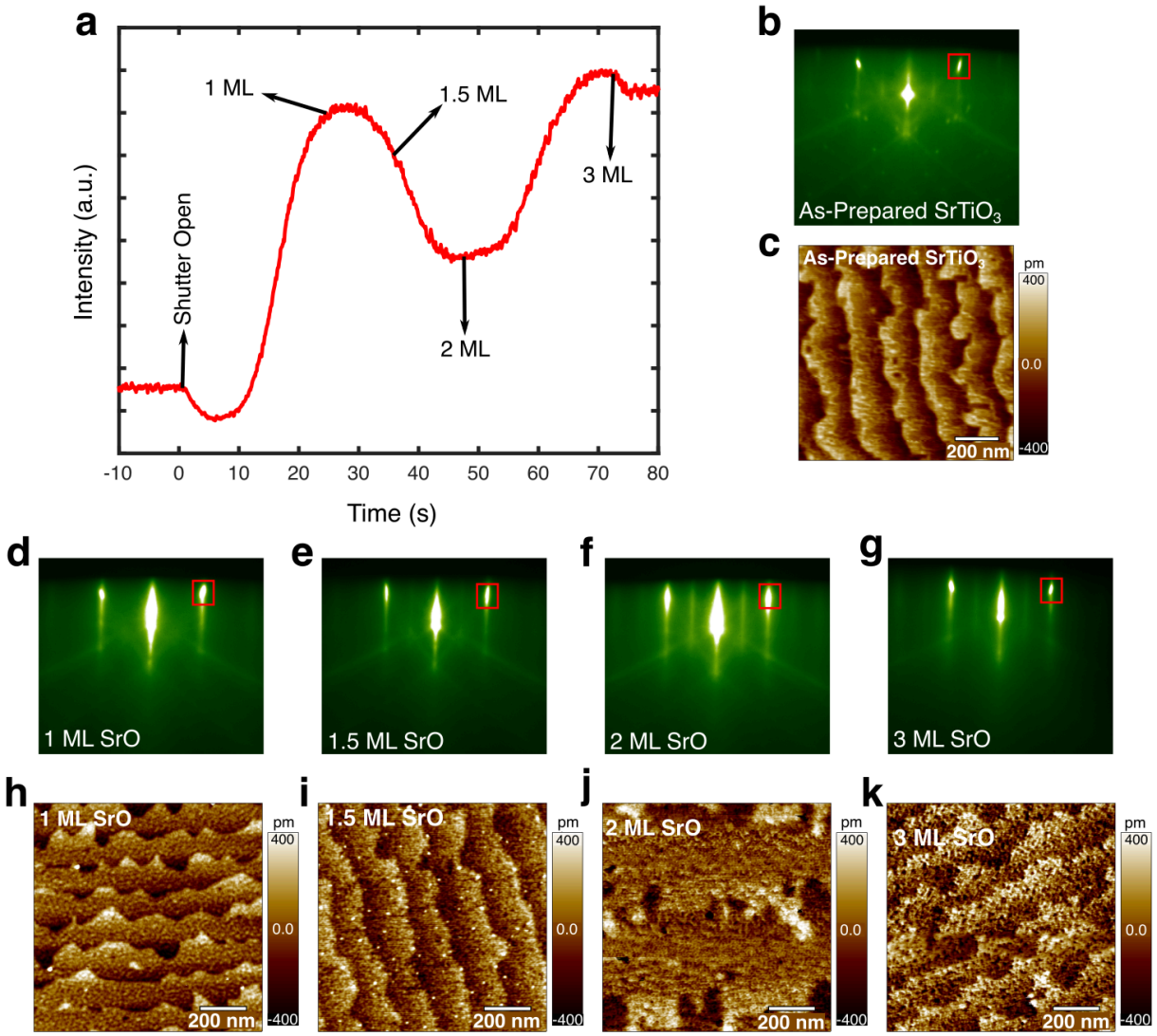

Figure S1 (a) Measurement of RHEED intensity as 3 monolayers (ML) of SrO are deposited on (001) $SrTiO_3$. **(b)** RHEED image of the as-prepared substrate along the SrTiO3 [110] azimuth at a substrate temperature of 775 °C and a background pressure of 5×10^{-7} Torr of (O_2 + ~10% O_3). **(c)** AFM image of the as-prepared substrate. **(d-g)** RHEED images and **(h-k)** AFM data collected on 1, 1.5, 2, and 3 monolayer (ML) thick SrO films on $SrTiO_3$.

II. Procedure for correcting flux drift

One of the most important aspects of the technique presented here is that monitoring the RHEED reconstruction during growth can provide insight into the drift in relative flux

(i.e., the *A*/Ti dosage ratio) during sample growth so that it can be adjusted. This is critical, particularly for relatively thick films, because fluxes always drift over time, usually on the order of 1% every 5-10 hours for our MBE system. The ability to respond to this drift enables much more efficient research, and *in situ* feedback could enable growth to be automated in an industrial setting.

To quantify the prevalence of the ½-order peak in the main text, we calculate the percentage of the perovskite cycle in which it is observed by generating a 2D plot of the line scan vs. time and measuring the distance (i.e., time) that the half orders are present compared to the total time. Because this is cumbersome in practice, we instead use the time it takes the ½-order to disappear during TiO_2 deposition and divide that by the total layer time, which can be measured and calculated quickly and easily. The slope of ½-order intensity vs. time is steeper during TiO_2 deposition than during SrO deposition (as seen in Fig. 1(b)), meaning the time of disappearance during TiO_2 can be judged more precisely than the time of appearance during SrO deposition. Measuring appearance vs. disappearance may give slightly different numbers, but using the same measurement consistently, it is possible to develop an effective and repeatable growth procedure.

The precise methodology our group employs to respond to drift is best explained by way of example. Say we intend to grow a 200 nm thick $(SrTiO_3)_{20}SrO$ film which takes almost 6 hours using the initial calibration: 20 seconds per monolayer dose for both SrO and TiO_2 at the source temperatures in use. In the first Ruddlesden-Popper unit cell, we would ensure that the ½-order streaks are present for ~80% of the last perovskite layer before the $(SrO)_2$ fault is crystallized (i.e., ½-order streaks disappear 16 seconds into the

final TiO_2 layer before the fault is deposited). After the recipe has run for 2 hours, we observe the ½-order streaks in RHEED near the end of the present Ruddlesden-Popper unit cell, and see that the ½-order streaks are present for only ~70% of each perovskite layer (i.e., ½-order streaks disappear 14 seconds into the TiO_2 layer). This means that the surface is ~10% SrO-deficient compared to the beginning of the growth. We respond by:

1. Fixing the surface of the growing film—Assuming we have no suspicions as to whether the strontium or titanium flux drifted, we adjust both doses to a single perovskite unit cell before the fault is crystallized to return to the optimum surface stoichiometry in which ½-order streaks disappear 80% into the final TiO_2 layer before the fault. More specifically, we would add 5% to the SrO dosage (21 seconds), and subtract 5% from the TiO_2 dosage (19 seconds) for a single perovskite unit cell to restore optimum surface stoichiometry.
2. Addressing the drift- After fixing the surface, we do not want to return to 20 second doses. Instead, we want to modify the doses to account for the observed drift. The procedure we have found most effective to evaluate drift is to divide the change in ½-order prevalence by *n*, which in this case would correspond to (80%-70%) ÷ 20 = 0.5% drift in the Sr/Ti flux ratio. The logic here is that a 0.5% error should modify the surface stoichiometry by 0.5% for each perovskite layer adding up to 0.5% × 20 = 10% deviation in surface stoichiometry during one Ruddlesden-Popper unit cell. Assuming we have no suspicions as to whether the strontium or titanium flux drifted, we would change

the shutter times of both sources equally to accommodate the drift: reducing the 20.0 second TiO_2 dosage by 0.25% to a 19.95 second TiO_2 dosage and increasing the 20.0 second SrO dosage by 0.25% to a 20.05 second SrO dosage.

While this correction resolves the drift in relative flux, the absolute flux is also relevant for the growth of Ruddlesden-Popper films. Interestingly, we do not find that the satellite peak intensity is very sensitive to errors in absolute flux, but structurally the average spacing between $(SrO)_2$ faults will be different from the ideal structure. As a result, intergrowths of other Ruddlesden-Popper series members (i.e., $n - 1$ or $n + 1$ phases) become more common in films that are grown with errant absolute flux calibration. We do not have an *in situ* method to monitor absolute flux with the required precision, but we developed an *ex situ* XRD technique to accurately measure the superlattice periodicity from which we can deduce the absolute flux (i.e., the dosage of Sr+Ti).[3] Thus, we cannot perfectly respond to flux drift in real time, but our relatively stable source fluxes combined with our iterative approach of *in situ* monitoring the relative flux followed by *ex situ* measurement of the absolute flux, enables consistent growth of Ruddlesden-Popper films with high structural quality.

III. Approximation of vertical fault density

From analyzing LAADF-STEM data of our $(SrTiO_3)_{50}SrO$ film in Fig. 3(b), we calculate that bright vertical lines, indicative of faults, occur every 5 nm on average. The simplest interpretation of this data is that the vertical fault density in the film is the inverse: 200 μm^{-}

[1]. Approximation of the vertical fault density using LAADF-STEM is complicated by the fact that most vertical faults do not extend through the entire lamella. We know that such faults are the majority because we observe primarily T-junctions between vertical faults and horizontal faults, which arise from vertical faults that do not extend through the entire lamella as discussed in the main text (Fig. 3(c-d)). Figure S2 shows plan-view diagrams of different vertical fault patterns that would yield bright contrast at the positions indicated by the black lines in a cross-sectional LAADF-STEM image. On average, there is 1 black line per 5 nm in these diagrams, consistent with the 1 fault per 5 nm observed with LAADF-STEM (Fig. 3(b)). The simplest interpretation of the LAADF-STEM image, assuming that faults pass through the entire lamella, is shown in Fig. S2(a). With this interpretation, one would deduce that the fault density (fault length per area in the plan-view diagram) is 200 μm^{-1}, much higher than the ideal horizontal fault density of 51 μm^{-1}. This interpretation is unreasonable, as the pattern of vertical faults shown in Fig. S2(a) breaks the 4-fold symmetry expected in the film, and this structure would not explain the T-junctions that are frequently observed in the LAADF-STEM image. The second diagram (Fig. S2(b)) is a more reasonable guess in which random vertical fault formation is isotropic and would result in many apparent T-junctions in the LAADF-STEM image. For this interpretation, the vertical fault density of 135 μm^{-1} is still well beyond that of the ideal horizontal fault density (51 μm^{-1}). If we instead hypothesize that the vertical fault formation is not random because it appears at the boundary between a crystallized horizontal fault and a region where no horizontal fault crystallized, we may speculate that the vertical fault structure looks as indicated in Fig. S2(c) with a relatively low density of

45 μm^{-1}. Even in this optimistic interpretation, the vertical fault density is comparable to the horizontal fault density observed in the film, leading us to conclude that the vertical fault density almost certainly exceeds the horizontal fault density of the film. Our best estimate is thus that the vertical fault density lies between the optimistic extreme of Fig. S2(c) and the random, isotropic case, Fig. S2(b). It is roughly 90 μm^{-1}, double that of the horizontal fault density.

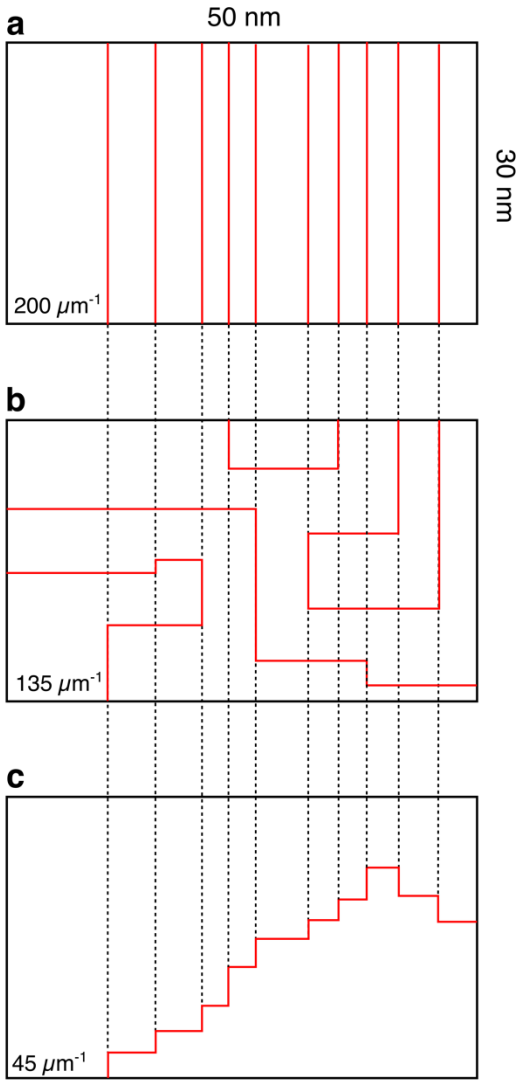

Figure S2 Plan-view diagrams of vertical fault patterns with a fault density of **(a)** 200 μm^{-1} **(b)** 135 μm^{-1} and **(c)** 45 μm^{-1}.